RESEARCH ARTICLE SUMMARY

ACTIVE MATTER

# Transition from turbulent to coherent flows in confined three-dimensional active fluids

**Kun-Ta Wu, Jean Bernard Hishamunda, Daniel T. N. Chen, Stephen J. DeCamp, Ya-Wen Chang, Alberto Fernández-Nieves, Seth Fraden,* Zvonimir Dogic***

**INTRODUCTION:** Conventional nonequilibrium systems are composed of inanimate components whose dynamics is powered by the external input of energy. For example, in a turbulent fluid, energy cascades down many length scales before being dissipated. In comparison, diverse nonequilibrium processes in living organisms are powered at the microscopic scale by energy-transducing molecular processes. Energy injected at the smallest scales cascades up many levels of structural organization, collectively driving dynamics of subcellular organelles, cells, tissues, and entire organisms. However, the fundamental principles by which animate components self-organize into active materials and machines capable of producing macroscopic work remain unknown. Elucidating these rules would not only provide insight into organization processes that take place in living matter but might lay the foundation for the engineering of self-organized machines composed of energy-consuming animate components that are capable of mimicking the properties of the living matter.

**METHODS:** We studied isotropic active fluids composed of filamentous microtubules, clusters of kinesin molecular motors, and depleting polymers. The polymer bundles microtubules, whereas the adenosine triphosphate (ATP)–fueled motion of kinesin clusters powers their extension. The extensile bundles consist of oppositely aligned polar microtubules and thus have quadrupolar (nematic) symmetry. They generate local active stresses that collectively drive mesoscale turbulent-like dynamics of bulk active fluids. Upon ATP depletion, the motion of microscopic motors grinds to a halt; the turbulent-like dynamics of active fluids ceases, and one recovers the behavior of conventional gels. We confined such active isotropic fluids into three-dimensional (3D) toroids, disks, and other complex geometries whose dimensions' range from micrometers to meters and studied their self-organized dynamics. Using particle tracking and image analysis, we simultaneously quantified the flow of the background fluid and the structure of the active microtubule network that drives such fluid flows.

**RESULTS:** We demonstrate that 3D confinements and boundaries robustly transform turbulent-like dynamics of bulk active fluids into self-organized coherent macroscopic flows that persist on length scales ranging from micrometers to meters and time scales of hours. The transition from turbulent to a coherently circulating state is not determined by an inherent length scale of the active fluid but is rather controlled by a universal criterion that is related to the aspect ratio of the confining channel. Coherent flows robustly form in channels with square-like profiles and disappear as the confining channels become too thin and wide or too tall and narrow. Consequently, this transition to coherent flows is an intrinsically 3D phenomenon that is impossible in systems with reduced dimensionality. For toroids whose channel width is much smaller than the outer radius, the coherent flows assume a Poiseuille-like velocity profile. As the channel width becomes comparable with that of the toroid outer diameter, the time-averaged flow velocity profile becomes increasingly asymmetric. For disk-like confinements, the inner two thirds of the fluid assumes rotation dynamics that is similar to that of a solid body. Analysis of the microtubule network structure reveals that the transition to coherent flows is accompanied by the increase in the thickness of the nematic layer that wets the confining surfaces. The spatial variation of the nematic layer can be correlated to the velocity profiles of the self-organized flows. In mirror-symmetric geometries, the coherent flows can have either handedness. Ratchet-like chiral geometries establish geometrical control over the flow direction.

ON OUR WEBSITE

Read the full article at http://dx.doi.org/10.1126/science.aal1979

**DISCUSSION:** Thousands of nanometer-sized molecular motors collectively generate a gradient in active stress, which powers fluid flow over meter scales. Our findings illustrate the essential role of boundaries in organizing the dynamics of active matter. In contrast to equilibrium systems in which boundaries are a local perturbation, in microtubule-based active fluid the influence of boundaries propagates across the entire system, regardless of its size. Our experiments also demonstrate that active isotropic fluids with apolar symmetry can generate large-scale motion and flows. From a technology perspective, self-pumping active fluids set the stage for the engineering of soft self-organized machines that directly transform chemical energy into mechanical work. From a biology perspective, our results provide insight into collective many-body cellular phenomena such as cytoplasmic streaming, in which molecular motors generate local active stresses that power coherent flows of the entire cytoplasm, enhancing the nutrient transport that is essential for the development and survival of many organisms. ■

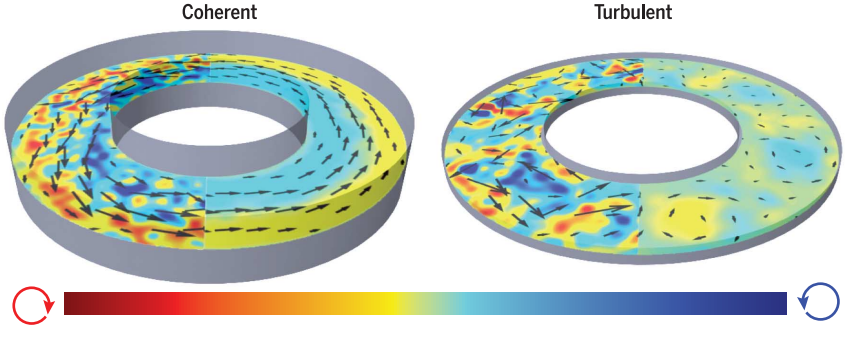


**Increasing the height of the annulus induces a transition from locally turbulent to globally coherent flows of a confined active isotropic fluid.** The left and right half-plane of each annulus illustrate the instantaneous and time-averaged flow and vorticity map of the self-organized flows. The transition to coherent flows is an intrinsically 3D phenomenon that is controlled by the aspect ratio of the channel cross section and vanishes for channels that are either too shallow or too thin.

The list of author affiliations is available in the full article online.
*Corresponding author. Email: fraden@brandeis.edu (S.F.); zdogic@brandeis.edu (Z.D.)
Cite this article as K.-T. Wu *et al.*, *Science* **355**, eaal1979 (2017). DOI: 10.1126/science.aal1979

RESEARCH ARTICLE

ACTIVE MATTER

# Transition from turbulent to coherent flows in confined three-dimensional active fluids

Kun-Ta Wu,[1] Jean Bernard Hishamunda,[1] Daniel T. N. Chen,[1] Stephen J. DeCamp,[1] Ya-Wen Chang,[2] Alberto Fernández-Nieves,[2] Seth Fraden,[1]* Zvonimir Dogic[1]*

**Transport of fluid through a pipe is essential for the operation of macroscale machines and microfluidic devices. Conventional fluids only flow in response to external pressure. We demonstrate that an active isotropic fluid, composed of microtubules and molecular motors, autonomously flows through meter-long three-dimensional channels. We establish control over the magnitude, velocity profile, and direction of the self-organized flows and correlate these to the structure of the extensile microtubule bundles. The inherently three-dimensional transition from bulk-turbulent to confined-coherent flows occurs concomitantly with a transition in the bundle orientational order near the surface and is controlled by a scale-invariant criterion related to the channel profile. The nonequilibrium transition of confined isotropic active fluids can be used to engineer self-organized soft machines.**

Conventional nonequilibrium pattern-forming systems, such as Rayleigh-Benard convection, are powered by continuous injection of energy through macroscopic external boundaries (*1*). In comparison, hierarchically organized living matter is driven away from equilibrium by the motion of microscopic energy-transducing animate constituents. Starting with molecular motors and continuing up to subcellular organelles, cells, tissues, and entire organisms, each biological element is constructed from energy-consuming components. At each level of hierarchy, these animate elements push and pull on each other, thus generating local active stresses. Collectively, these stresses enable diverse functionalities that are essential for survival of living organisms, such as cell division and motility (*2*–*8*). Under geometrical confinements, active building blocks such as motile cells, tissues, and organisms can also organize into coherently moving nonequilibrium states (*9*–*17*). Creating active matter systems from the bottom up that mimic the remarkable properties of living matter remains a fundamental challenge (*18*–*20*). Recent studies have revealed the emergence of diverse complex patterns in synthetic systems of active matter (*21*–*26*). The next step is to elucidate conditions that transform chaotic dynamics of these systems into coherent long-ranged motion that can be used to harvest energy and thus power various micromachines (*27*–*32*).

Here, we study three-dimensional (3D) active fluids and demonstrate an essential difference with their conventional counterparts. The Navier-Stokes equations dictate that a conventional fluid composed of inanimate constituents will flow only in response to an externally imposed body force, or stress and pressure gradients (*33*). This is no longer true for active fluids. In living organisms, the entire cellular interior can assume large-scale coherent flows in absence of any externally imposed stresses, a phenomenon known as cytoplasmic streaming (*34*–*36*). Despite recent advances using living bacterial suspensions (*12*, *13*, *17*, *37*), creating tunable synthetic active fluids that exhibit autonomous long-ranged flows on length scales large compared with those of constituent units remains a challenge. We use a 3D microtubule-based isotropic active fluid whose bulk turbulent flows are driven by continuous injection of energy through the linear motion of the constituent kinesin motors (*24*, *38*). We found that confinement robustly transforms locally turbulent dynamics of such active fluids into globally coherent flows that persist on meter scales. Our experiments demonstrate that nonequilibrium transitions of synthetic active materials can be used to engineer self-organized machines in which nanometer-sized molecular motors collectively propel fluid on macroscopic scales.

## Microtubule-based active isotropic fluids

The active fluid we studied comprises microtubule filaments, kinesin motor clusters, and depleting polymer (Fig. 1A) (*24*, *38*). Kinesin motors are bound into synthetic clusters with tetrameric streptavidin (*39*, *40*). The depleting polymer induces microtubule bundling (*41*), while the kinesin clusters simultaneously bind to and move along the neighboring filaments. For aligned microtubules with opposite polarity, kinesin clusters generate interfilament sliding that drives the flow of the background fluid (Fig. 1A) (*42*). At finite concentrations (≥0.5 mg/mL), active microtubule bundles form a self-rearranging 3D isotropic network, whose dynamics comprise repeating cycles of bundles extending, buckling, fracturing, and annealing. Such dynamics effectively drives the flow of the background fluid that is mostly composed of an aqueous buffer (~99.9%). In bulk suspensions, microtubule-based active networks generate turbulent-like flows that exhibit neither long-range order nor net material transport. The structure of these flows and the associated vorticity fields are visualized by doping active fluids with fluorescent tracer particles (Fig. 1D and Movie 1). Such analyses reveal a characteristic vortex size of ~100 μm, with an average lifetime of ~3 s.

Energy-efficient kinesin motors allow for assembly of bulk 3D active fluids that maintain steady-state turbulent flows for up to 10 hours. This feature allows us to quantify the time-average of various steady flows. Furthermore, filamentous microtubules effectively couple to the background fluid. Therefore, even at volume fractions as low as 0.05%, the microtubule network drives the bulk turbulent flows. At such low concentrations, the network has a very large pore size (~10 μm); thus, its structure can be visualized and quantitatively analyzed with optical microscopy. This property allows us to correlate the

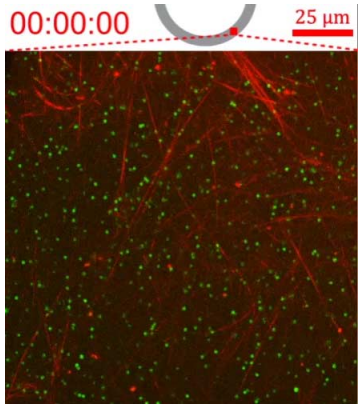


**Movie 1. Motion of toroidally confined active microtubules (red) and tracer particles (green).** Height and width of the toroid are 80 and 200 μm, respectively. The movie was taken with a confocal microscope, and microtubules and bead tracers are indicated in red and green, respectively. To visualize flow at a higher resolution, the concentration of traced beads is increased to ~0.01% v/v. Flow rates of microtubules and tracers reveal no measurable differences. Time stamp is hour: minute: second.

[1]Department of Physics, Brandeis University, 415 South Street, Waltham, MA 02453, USA. [2]School of Physics, Georgia Institute of Technology, 837 State Street, Atlanta, GA 30339, USA.
*Corresponding author. Email: fraden@brandeis.edu (S.F.); zdogic@brandeis.edu (Z.D.)

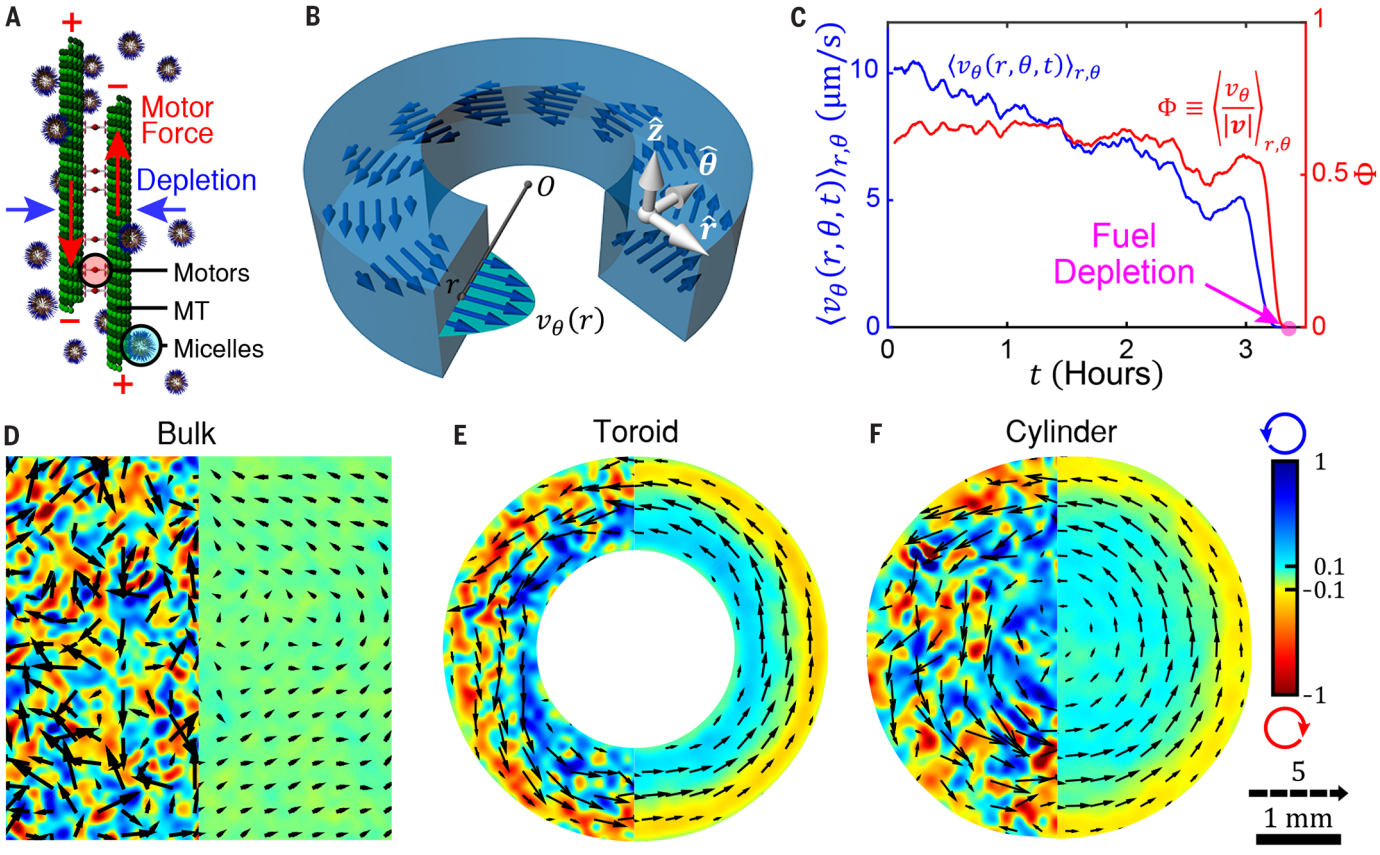


**Fig. 1. Coherent macroscopic flows of confined active fluids.** (**A**) The three main constituents of an active fluid: microtubules; kinesin clusters, which power interfilament sliding; and pluronic micelles, which act as a depleting agent. (**B**) Schematic of a coherent flow that emerges when active fluids are confined in a toroid. (**C**) Time evolution of the averaged azimuthal velocity (blue) and the circulation order parameter (red) demonstrates that circular flows cease upon ATP depletion. (**D**) A flow map demonstrates that bulk active fluids exhibit turbulent flows that do not transport material. The vector field indicates the local flow velocity normalized by the mean flow speed. The color map represents the normalized vorticity distribution, with blue and red tones representing CCW and CW vorticities, respectively. Left and right halves are instant and time-averaged plots, respectively. (**E**) An active fluid in a toroidal confinement exhibits persistent circular flows. (**F**) Coherent flows in a cylindrical confinement. Confinement heights are 1.3 mm. (D) to (F) share the same scale, velocity, and color bars.

properties of the emergent flows to the structure of the underlying active network.

### Confinement-induced coherent flows

We found that 3D toroidal confinements can effectively transform directionless turbulent flows of bulk fluids into coherent circular currents capable of transporting materials over macroscopic scales (Fig. 1, B and E). Similar phenomena were also observed for cylindrical confinements, demonstrating that toroidal geometry is not an essential requirement for the formation of coherent flows (Fig. 1F). The autonomous circular currents persisted for hours and ceased only after the available chemical energy [adenosine triphosphate (ATP)] is depleted (Fig. 1C). The flow coherence was quantified by the order parameter $\Phi \equiv \langle v_\theta/|v|\rangle$, where $v_\theta$ is the flow velocity along the azimuthal direction ($\hat{\theta}$) and $|v|$ is the flow speed. $\Phi = 1$ indicates perfect circular flows, whereas $\Phi = 0$ indicated no net transport along the tangential direction. We measured $\Phi \sim 0.6$, and the magnitude of the order parameter remained fairly constant over the entire sample lifetime (Fig. 1C).

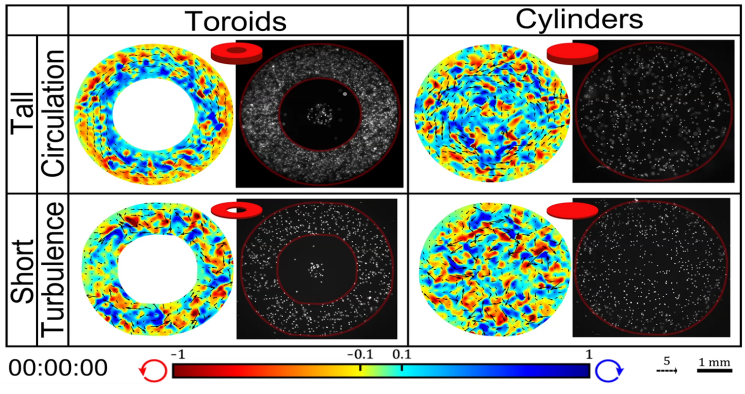


**Movie 2. Coherent and incoherent flows in toroids and cylinders.** Flows of active fluids in toroidal and cylindrical confinements that support and suppress coherent flows. Increasing confinement height induces a transition from incoherent to coherent flows. Heights of taller toroid (top left) and cylinder (top right) are 1.3 mm, and heights of shorter ones (bottom left and right) are 0.33 mm. Black vectors and color maps (left half in each panel) represent fluid velocity fields and vorticity distributions extracted from the motion of tracer beads (right half). Time stamp is hour: minute: second.

Not all geometries support coherent flows. For example, reducing the height of a toroid or a cylinder below a critical value completely suppressed coherent flows and yielded turbulent-like dynamics (Movie 2 and fig. S1). To determine geometries that support self-organized circular

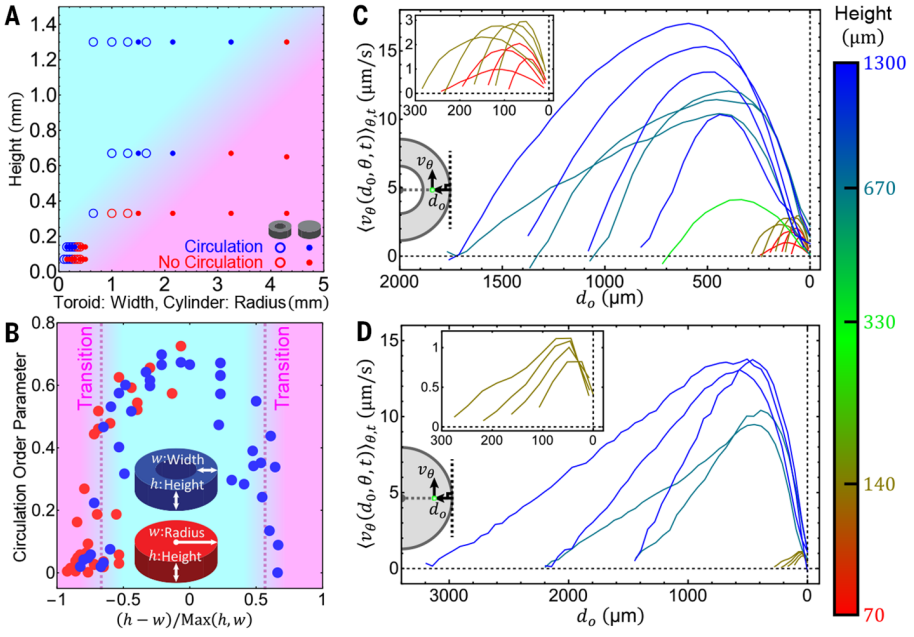


**Fig. 2. Phase diagram and velocity profiles of coherent flows in toroids and cylinders.** (**A**) A phase diagram indicating confinement geometries that support circular flows. The phase diagram is limited to thin confining geometries, $h \leq 2w$. Circles and dots represent toroidal and cylindrical confinements, respectively. (**B**) The circulation order parameter, Φ, as a function of the confinement aspect ratio, $\alpha \equiv (h - w)/\mathrm{Max}(h, w)$. $\alpha = 0$ represents a square cross section. Blue and red dots represent toroids and cylinders, respectively. For $\alpha < 0.5$, Φ was measured at midplane. For $\alpha > 0.5$, Φ was measured at a quarter plane because of the finite working distance of the microscope objective. (**C**) Flow velocity profiles in various toroidal confinements taken at a midplane. Outer diameters of toroids for blue, teal, and green curves are 4300 μm and for olive and red curves are 2000 μm. (Inset) Flow profiles of toroids with width ≤300 μm. (**D**) Midplane flow profiles in various cylindrical confinements. (Inset) Flow profiles in cylinders with radius ≤300 μm. The color bar on the right indicates the confinement heights.

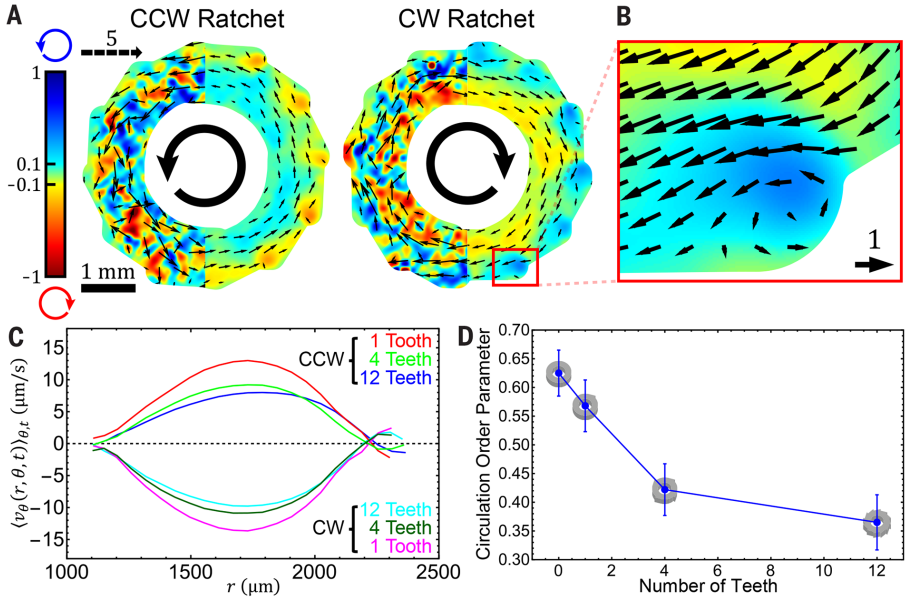


**Fig. 3. Controlling flow of coherent handedness.** (**A**) The handedness of the circular flows is controlled by decorating the toroid's outer surface with counterclockwise or clockwise ratchets. The vector and color maps represent the local flow velocity and vorticity. (**B**) Velocity field and vorticity maps demonstrate that each notch induces a stationary vortex. (**C**) Midplane flow profiles in CCW and CW ratchets with varying notch numbers. Backflow from ratchets occurs near the outer edge, radius ($r$) ≈ 2300 μm. All channel heights are 1.3 mm. (**D**) The circulation order parameter as a function of the number of notches.

flows, we varied the widths, heights, and radii of toroids with rectangular cross sections as well as radii and heights of the cylindrical geometries (Figs. 2A). From an extensive data set, we draw the following observations: First, self-organized flows are robust, occurring over a range of confining geometries whose volumes span more than four orders of magnitude (from 0.006 to 18 μL). This range could be larger because we have determined neither the upper nor the lower volume that supports circular flows. Second, the self-organized circular flows are equally likely to be left- or right-handed. Third, for both toroids and cylinders, coherent flows diminish as the confining geometry becomes either too wide or too tall—that is, when the ratio of the long to short side of the channel cross section becomes greater than ~3. Sample-to-sample variation in the circulation order parameter was too great to determine whether the transition was continuous or discontinuous.

To quantify this observation, we plotted the circulation order parameter Φ as a function of the aspect ratio of toroids or cylinders: $\alpha \equiv (h - w)/\mathrm{Max}(h, w)$, where $h$ and $w$ are the height and width, respectively, of either a cylinder or toroid and Max($h$,$w$) represents their larger value (Fig. 2B). Geometries with square-like profiles ($\alpha = 0$) support robust flows. As the geometry becomes wider and/or shorter ($\alpha < 0$), the circulating flows only formed for cross sections that were sufficiently symmetric ($-0.6 < \alpha < 0$); otherwise, no net flows were observed. In the complementary regime of tall and narrow confinements ($\alpha > 0$), we observed a second transition from coherent to turbulent flow as the confinement geometry became taller or narrower ($\alpha > 0.6$). This observation demonstrates the equivalency between the height and width (or vorticity and gradient direction) of the confining geometry.

We observed flows over a well-defined range of the parameter α ($-0.6 < \alpha < 0.6$). This criterion appears to be universal because it holds for both micrometer- and millimeter-scale confinements as well as for toroidal and cylindrical geometries. The largest channels for which this criterion was established had a cross section of about a centimeter; further experimentation is required to establish whether there is an upper bound above which the criterion breaks down. This data suggest that the transition to coherent flows is not controlled by the intrinsic length scale of the bulk fluid, which is the vortex size of 100 μm (Fig. 1D), but rather by the dimensionless aspect ratio, α. For example, coherent circular flows are observed in cylinders with $w$ = 3.3 mm, which is 30 times larger than the vortex size of the bulk fluid. This is contrary to previous studies that determined the need to confine flows smaller than the intrinsic length scale of the bulk system (*12*, *17*). The criterion we uncovered demonstrates that the transition to coherent flows is an intrinsic 3D phenomenon that cannot, even in principle, exist in 2D systems. As the channel height is reduced to the 2D limit ($h \to 0$), the confinement parameter reduces to a single value, $\alpha \to -1$, which is in the regime in which coherent

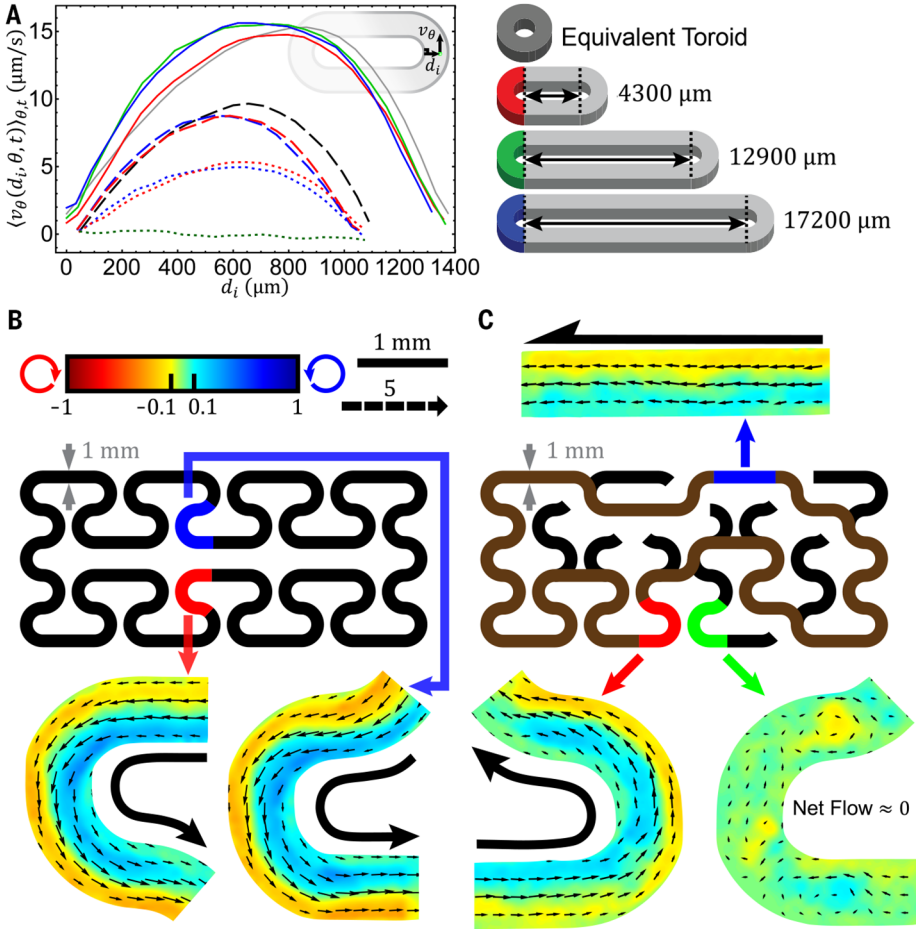


**Fig. 4. Circulating flows in closed tracks.** (**A**) Velocity profiles of coherent flows in racetrack geometries are independent of the length of the straight segment (solid curves). (**B**) Coherent flow in a 200-mm-long racetrack. Because of limited observation windows, we only observed the blue and red segments whose flow profiles are dashed same-color curves in (A). The fluids in these segments flow as fast as in an equivalent toroid whose $w = 1$ mm and $h = 1.3$ mm [dashed black curve in (A)]. (**C**) Self-organized flows can solve a 2D maze consisting of a closed loop (brown) and 10 dead-end branches (black). We observed only the blue and red segments in the close loop and the green segment in one branch. Their flow profiles are the dotted same-color curves in (A). Dead-end branches inhibit net transport, whereas the closed loop supports a persistent circulating flow. All channel heights are 1.3 mm.

flows do not occur (Fig. 2B). In other words, the scale-invariant criterion does not exist in two dimensions because there is only one channel dimension ($w$) perpendicular to the flow. In contrast, in 3D systems, the cross section has two dimensions ($h$, $w$), making it possible to construct a dimensionless aspect ratio that controls the onset of the coherent flows.

### Structure of the coherent flows

To quantify the spatial structure of the self-organized circular flows, we measured time-averaged azimuthal velocity profiles $\langle v_\theta(r)\rangle$ in both toroidal and cylindrical geometries. For small toroidal widths ($w < 1000$ μm), coherent flows exhibited Poiseuille-like symmetric profiles, with a peak velocity at the channel midpoint and decreasing to zero at the boundary because of the no-slip condition (Fig. 2C). The peak velocity increased with channel height. For a 330-μm-high and 650-μm-wide toroid, the maximum velocity was ~4 μm/s. Increasing the height to 1300 μm, for the same width, increased the peak velocity to ~10 μm/s. For the largest toroids studied, peak velocities reached ~17 μm/s, whereas for smallest micrometer-sized ones, peak velocities were as small as ~1 μm/s (Fig. 2C, inset). The asymmetry of the time-averaged velocity profile increased with increasing toroid width. The asymmetry became especially pronounced for cylindrical geometries in which the velocity increased from zero at the disk center, growing linearly to a maximum value before decreasing rapidly to zero at the outer edge (Fig. 2D). Such a distinguishing feature is universal for both micrometer- and millimeter-sized cylinders, indicating again that the flow structure is independent of the confinement size.

### Controlling handedness of coherent flows

In mirror-symmetric toroids and cylinders, coherent flows are equally likely to be either counterclockwise

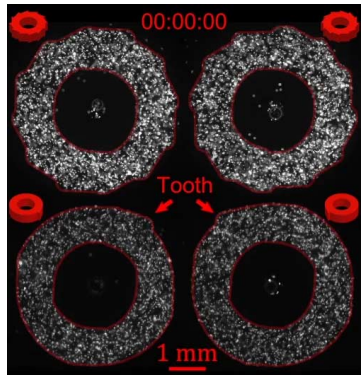


**Movie 3. Coherent flows in 12- and 1-tooth CCW and CW ratchets.** Decorating the toroid outer surface with notches induced coherent flows in the direction of same handedness. Even one notch is sufficient to control flow direction. The notch sizes are ~300 μm. Top two ratchets (left, CCW; right, CW) have 12 teeth, and bottom ones (left, CCW; right, CW) have only 1 tooth. Heights are 1.3 mm. Time stamp is hour: minute: second.

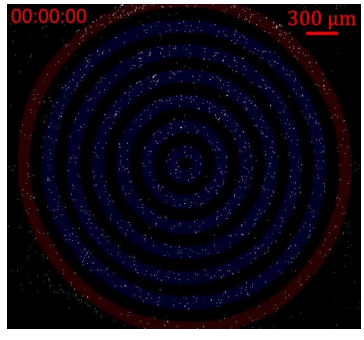


**Movie 4. Coherent flows in concentric micrometer-sized toroids.** Toroids' outer radii range from 175 to 1525 μm. Varying the radii does not alter flow rates, implying that coherent flow is independent of channel curvature. Tracks are shaded in blue and red for CCW and CW coherent flows. Channel heights are 60 μm. Time stamp is hour: minute: second.

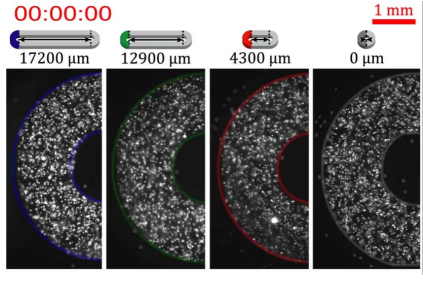


**Movie 5. Coherent flows in racetracks with varying circumferences and an equivalent toroid.** Varying circumferences does not alter flow rate, implying that coherent flow is independent of channel length. The lengths of straight paths from left to right are 17,200, 12,900, 4300, and 0 μm, respectively. Heights and widths in the racetracks and toroid are both 1.3 mm. Time stamp is hour: minute: second.

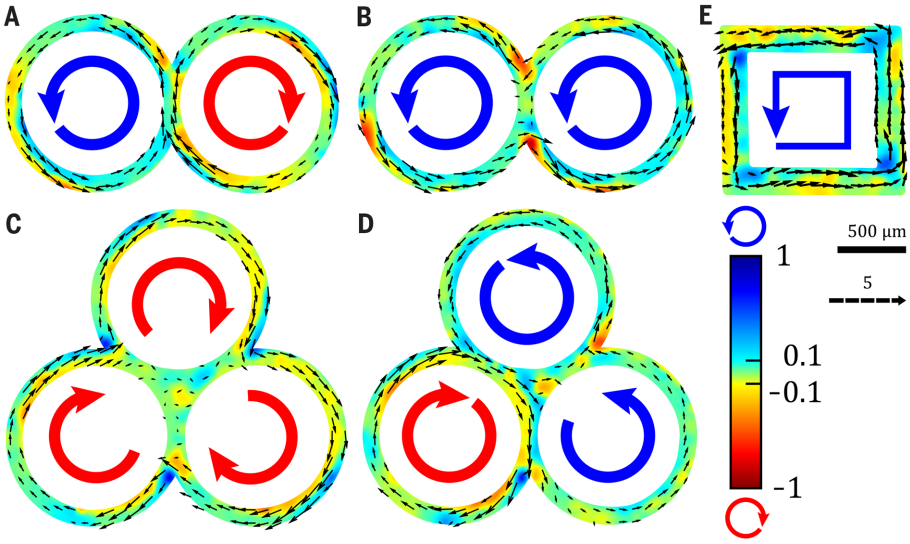


**Fig. 5. Coherent flows in miscellaneous confinements.** (**A** and **B**) Two distinct flow configurations in a pair of partially overlapping toroids. Confinement heights are ~60 μm. (**C** and **D**) Flow paths in three partially overlapping toroids. Confinement heights are ~60 μm. (**E**) Coherent flows in a square-like confinement. Channel height is ~75 μm.

(CCW) or clockwise (CW). To control the flow handedness, we decorated the toroid outer edge with sawtooth notches, finding that a CCW geometry induces flows of same handedness and vice versa (Fig. 3A and Movie 3). In contrast, decorating inner edges with the same pattern leads to flows with opposite handedness (fig. S2, A and B). Coherent flows could be completely suppressed by decorating both inner and outer surfaces with notches of the same chirality (fig. S2, C and D). Decreasing the number of notches increased the circulation order parameter, Φ, and even a single notch controlled the flow direction (Fig. 3D). Flow maps reveal that each notch creates a stationary vortex (Fig. 3B), and the back-flow associated with this vortex decreases the overall flow coherency (Fig. 3C).

We explored how the self-organized flow rates scale with the channel curvature and length, by either changing the toroid radii or stretching toroids into shapes resembling racetracks while maintaining the same cross section. The toroidal radius (curvature) does not affect the properties of the self-organized flows (Movie 4 and fig. S3). For racetrack geometries, we varied the total circumference length from 14 to 48 mm (Fig. 4A and Movie 5). Flow profiles in these geometries were nearly identical, demonstrating not only that the flow rate is independent of the pipe length but also that the straight and curved segments of a racetrack provide equal driving power. To further confirm this finding, we designed a 20-cm-long track (Fig. 4B). Coherent flow persisted in such a lengthy track; its rate remained nearly the same as that in a toroid of equivalent cross-section but shorter circumference (Fig. 4A).

## Coherent flows in complex confinements

The self-organized coherent flows are remarkably robust self-organized patterns. To determine limits of their stability, we explored emergent dynamics in geometries of increasing complexities. First, coherent flows developed not only in simple toroids but also in a complex maze-like geometry comprising a closed loop and many dead-end branches (Fig. 4C). Upon filling such geometry with active fluid, coherent flows developed in the closed loop while remaining turbulent in the dead-end branches. However, unlike racetrack geometries, the flow rate was ~50% slower than in an equivalent toroid, indicating that the dead-end branches disturb the self-organized flows (Fig. 4A). Second, we explored flows that emerge in two or three adjoining toroids and found that such geometries support multiple self-organized states (Fig. 5 and Movie 6). For example, in one state, flows in the two adjoining toroids had opposite handedness and were thus reinforced in the mutually adjoining region (Fig. 5A). In another state, the flow organized along the outer edge of the toroid doublet, therefore suppressing coherence in the adjoining region (Fig. 5B). Similarly, in triplet geometry we observed either flow circulating along the outer edge, leaving the center quiescent (Fig. 5C), or CW flow in one toroid and CCW flow in the other two (Fig. 5D). Third, coherent flows also developed in confinements with sharp corners, such as a square-like geometry (Fig. 5E). However, sharp corners induced formation of stationary vortices, which generated back-flow, thus decreasing the circulation order parameter, when compared with a toroid with an equivalent cross section. Last, we found that the self-organized flows are not limited to microfluidic channels. For example, active fluids exhibited macroscopic flows both within a torus inscribed within a finite yield-stress elastomer (fig. S4) (*43*), as well as a 1.1-m-long plastic tube (Fig. 6).

## Structure of the microtubule network

To elucidate the microscopic mechanism that drives coherent flows, we imaged the microtubule network structure of active fluids in both turbulent and coherent states and extracted the orientational distribution function (ODF) of the constituent bundle segments (Fig. 7A and Movies 7 and 8) (*44*). In the channel center, the measured ODFs were isotropic in both the coherent and turbulent states (indistinguishable from ODFs of bulk active fluids) (Fig. 7B). Emergence of the coherent flows was correlated with the change in the thickness of the nematic layer that wets the surfaces. We measured the spatial variation of the nematic order parameter in the direction perpendicular to the confining wall (Fig. 7C). In turbulent states, the nematic order decays away from the boundaries with a characteristic length

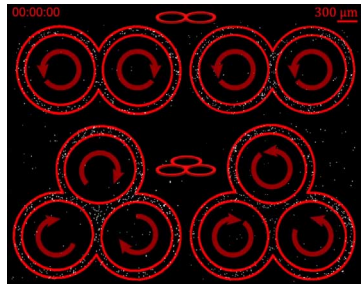


**Movie 6. Circulations in two (doublet) and three (triplet) connected toroids.** Fluids in the doublet can develop a CCW and CW circulations (top left) or two CCW circulations (top right). In three adjoining toroids, fluids can flow in the outer edge while leaving center quiescent (bottom left) or develop two CCW and one CW circulations (bottom right). Channel height is ~60 μm. Time stamp is hour: minute: second.

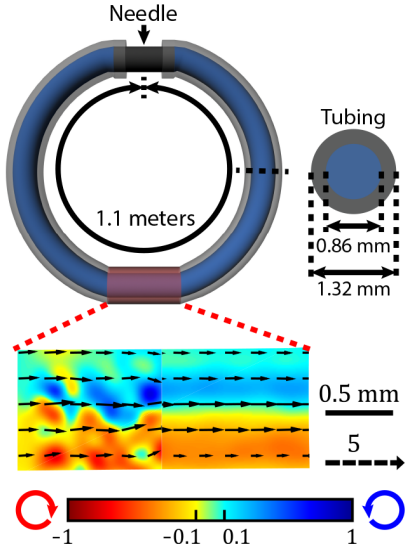


**Fig. 6. Active fluids flow on macroscopic scales.** An active fluid confined within a 1.1-m-long flexible tube with a circular cross section of 0.86 mm exhibits persistent flows. The red segment highlights the tube portion where fluid flows were observed and quantified.

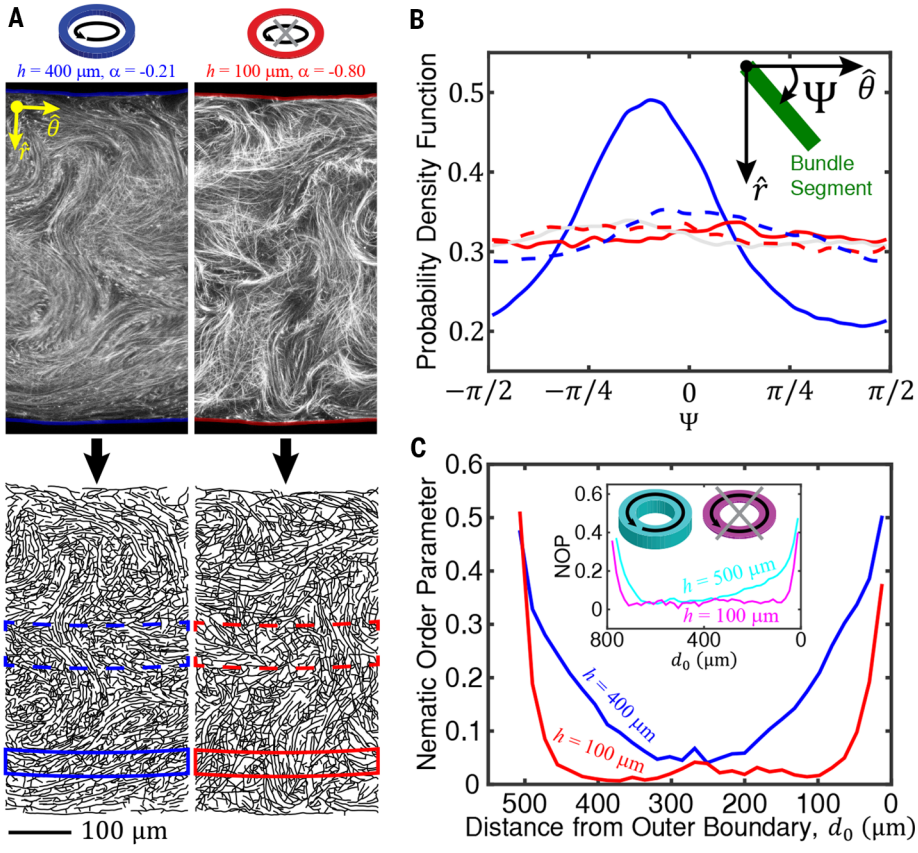


**Fig. 7. Transition to coherent flows correlates with the thickness of the nematic-wetting layer.** (**A**) (Top) Fluorescence images of a microtubule network that drives the coherent and turbulent fluid flows taken at the channel midplane. (Bottom) Reconstruction of the microtubule network that drives flow of active fluids in both the coherent and turbulent phase. (**B**) ODFs of microtubule bundle segments in the coherent (blue) and turbulent (red) state shown in (A). The solid curves indicate ODFs near the channel's outer boundary, whereas the dashed ones are measured at the channel center [solid and dashed boxes, respectively, in (A)]. The gray curve represents an isotropic suspension confined in a cuboid whose width = 18,000 μm, length = 14,000 μm, and height = 90 μm. (**C**) NOP profile across the channel width. (Inset) NOP profiles across 800-μm-wide toroids in coherent (light blue) and turbulent (pink) states.

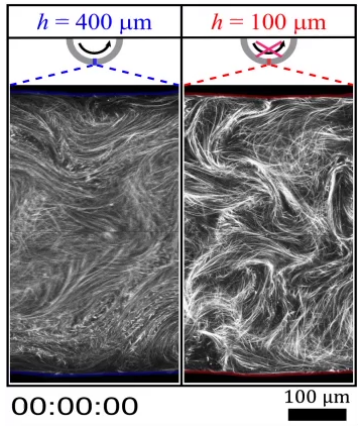


**Movie 7. Coherent (left) and incoherent (right) motion of active microtubule networks confined in toroids.** In a thin toroid (right, $h$ = 100 μm), microtubules move irregularly. Increasing confinement height to $h$ = 400 μm triggers a self-organized transition from turbulent to coherent flows (left). Time stamp is hour: minute: second.

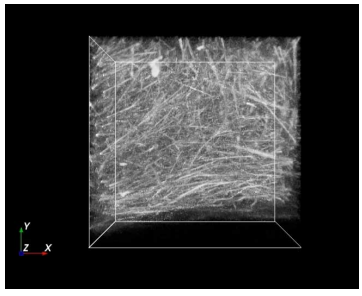

**Movie 8. Demonstration of using SOAX to analyze 3D bundle structure.** Magenta curves represent snakes that profile microtubule bundles; green dots represent their intersections. By using SOAX, bundle structures can be extracted from their confocal $z$-scanned images. Height, width, and outer diameter of the toroid are 100, 200, and 2000 μm, respectively.

scale ($l$ ~ 30 μm). Transition to coherent flows is accompanied with an increase in the thickness of the surface-induced nematic layer ($l$ ~ 100 μm). Similar to fluid flow profiles (Fig. 2C), lateral profiles of nematic order were asymmetric for circulating toroids with wide cross sections, whereas they were symmetric for narrow ones (Fig. 7C, inset), implying that the shear rates generated by coherent flows drive the filament alignment. The angle between the confining surface and the self-organized nematic layer had a finite nonzero value of ~20° (Fig. 7B), suggesting that active stresses generated by the spatially distorted wall-bounded nematic layer push against the no-slip boundary and thus propel the fluid forward (*45*).

## Discussion

We demonstrated that confining boundaries transform turbulent dynamics of bulk isotropic active fluids into long-ranged coherent flows. Our results suggest a mechanism by which this transition takes place. In conventional isotropic liquid crystals, the bounding surface breaks the local symmetry and locally aligns the constituent particles (*46*). In active systems, turbulent flows enhance this effect, magnifying and extending the wall-induced nematic order. We suggest that the nematic-wetting layer aligns to the surface at an oblique angle, thus generating an active surface stress that induces further flows. In turn, these flows further enhance and stabilize the orientation of the wetting layer. This positive feedback loop yields a cooperative nonequilibrium transition to globally coherent flows, reminiscent of a phenomenon known as "backflow" in conventional liquid crystals, in which mutually reinforcing coupling between the reorienting nematic director and the fluid velocity leads to emergent periodic structures (*47*, *48*).

Emergence of coherent flows is determined by a universal scale-invariant criterion, which is related to the aspect ratio of the confining channel cross section rather than the overall size of the confining geometry. In particular, coherent flows take place when the channel cross section is relatively symmetric—that is, the width and height of the channel are within a factor of 3 of each other. Understanding the onset of large-scale flows is a central focus of active matter research. One class of theoretical models predicts an active Fréedericksz transition from quiescent to coherent flows for monodomain active liquid crystals (*27*, *28*, *49*, *50*). There are several notable differences between our observations and the active Fréedericksz transition. First, our phenomenon is inherently 3D. That the aspect ratio alone, and not the absolute channel size, controls the onset of coherent flows forbids this transition from taking place in systems with lower dimensionality. This restriction does not hold for the active Fréedericksz transition, which can occur in two dimensions. Second, in our experiments the coherent flows form in an active isotropic fluid, instead of a liquid crystalline one. Third, the flows we observed also emerged from the turbulent state, whereas the active Fréedericksz transition predicts the formation of such flows from a quiescent, single-domain nematic.

The boundary-generated active stresses power coherent flows. This bears similarity to electroosmosis, in which an external electric field creates boundary-layer stresses that lead to plug flow (*51*). The time-averaged coherent flows of active matter confined in cylinders, in which the interior fluid away from the interface moves as a solid body, resemble such plug flows. However, there are also notable differences. The velocity of electroosmotic plug flow is independent of channel size when the boundary layer is small. In contrast, we observed that the coherent active flow velocity varies with channel size. Additionally, active flows in tori resemble Poisuille flow, indicating pressure-driven flow.

The possible relevance of our mechanism to cell biology still has to be ascertained. In particular, coherent cytoplasmic flows in living cells are powered by cytoskeletal filaments that are permanently affixed at the cellular cortex (*34*–*36*), whereas in our system, the active elements are dispersed throughout the sample interior and dynamically self-organize at the solid boundaries that confine the fluid.

We demonstrate that nonequilibrium transitions in active matter can be used for the robust assembly of self-organized machines that produce useful work by powering large-scale fluid flow. These machines are fueled by the collective motion of the constituent nanometer-sized motors and are thus evocative of living organisms. However, the goals of active matter research are not only to recreate materials found in nature but additionally are to discover and elucidate the full range of dynamical organization that is possible in living and nonliving systems alike. Toward this end, explaining the scale-invariant criterion for the onset of coherent flows and their velocity profiles represents a challenge for active matter theory.

## Materials and methods

### Assembling kinesin clusters

We used kinesin motors dimers comprising a 401-amino acid N-terminal domain derived from *Drosophila melanogaster* kinesin labeled with a 6-his tag and a biotin tag. Kinesin motors were purified according to a previously published protocol (*52*). An isolated kinesin moves along a single microtubule protofilament toward its plus end. Linking kinesins into multimotor clusters enables them to bind multiple microtubules and drive interfilament sliding. The biotin-labeled motors were assembled into multimotor clusters using streptavidin tetramers. To assemble kinesin clusters, we mixed 1.5 μM kinesin motors with 1.8 μM streptavidin (Invitrogen, S-888) at a 1:1.2 ratio in microtubule M2B buffer (M2B: 80 mM PIPES, pH 6.8, 1 mM EGTA, 2 mM $MgCl_2$) containing 120 μM dithiothreitol (DTT). The mixture was then incubated for 30 min at 4°C, before being aliquoted and stored long-term at -80°C.

### Microtubule polymerization

Tubulin monomers were purified from bovine brains with two cycles of polymerizations and depolymerizations in a high salt buffer (1 M PIPES buffer), followed with one cycle in M2B buffer (*53*). To induce polymerization, the tubulin suspension (8 mg/mL in M2B) was mixed with 600 μM GMCPP (guanosine-5′-[(α,β)-methyleno] triphosphate, Jena Biosciences, NU-4056) and 1 mM DTT. For fluorescence imaging, 3% of tubulin monomers were labeled with Alexa-Fluor 647 (Invitrogen, A-20006). The tubulin mixture was first incubated for 30 min at 37°C, followed by an annealing step at room temperature for six hours. The resulting microtubules have an average length of ~1 μm (*24*). The polymerized microtubules were stored at -80°C.

### Microtubule-based active fluids

To assemble active fluids, 1.3 mg/mL microtubule suspension was mixed with kinesin-streptavidin motor clusters in a high-salt M2B (M2B + 3.9 mM $MgCl_2$) (*24*). Kinesin motors hydrolyze adenosine triphosphate (ATP) into an adenosine diphosphate (ADP) while stepping toward the microtubule plus end. To fuel such motion we added 1.4 mM ATP. To maintain constant ATP concentration and steady dynamics in active fluids, we have incorporated an ATP regeneration system comprising 26 mM phosphoenol pyruvate (PEP) and 2.8% v/v stock pyruvate kinase/lactate dehydrogenase enzymes (PK/LDH) (Sigma, P-0294) (*54*). PK consumes PEP and converts ADP back to ATP, thus maintaining steady ATP concentration. To reduce photo-bleaching effects during fluorescence imaging, we added 2 mM trolox (Sigma, 238813) and an oxygen scavenging enzyme mixture comprised of 0.22 mg/mL glucose oxidase (Sigma, G2133), 0.038 mg/mL catalase (Sigma, C40), and 3.3 mg/mL glucose. To stabilize proteins we added 5.5 mM DTT as a reducing agent. As the depletion agent we used 2% w/w Pluronic F127, which assembles into ~20 nm micelles (*55*). Finally, to track the flow induced by active fluid, we added ~0.0004% v/v Alexa 488-labeled 3-μm polystyrene particles, stabilized by Pluronic F127. Upon mixing all of the above ingredients, nonequilibrium dynamics of active fluids can last for hours, until both ATP and PEP are depleted.

### Engineering microfluidic chips

Millimeter-scale (≥0.3 mm) devices were manufactured by directly milling a 2-mm-thick COC plaque (TOPAS Advanced Polymers) with a CNC end-milling machine, which reads G-code translated from CAD with Cut2D (Vectric). Micron-scale devices were manufactured by embossing COC plaques (thermoplastic polymers) with patterned polydimethylsiloxane (PDMS, thermosetting polymers) slabs at ~180°C (*56*). The slabs were molded by casting uncured PDMS resin (1:10 ratio of curing agent to base, Dow Corning) on a standard SU8 master and baked at 70°C overnight. The master was photo-lithographed with photomasks printed from CAD. Millimeter- and micron-scale devices were subsequently cleaned with ethanol by a ~5-min sonication, followed by a ~20-min sonication in water. To protect proteins from direct surface contact, the COC chips were precoated with polymer brushes. Since COC is hydrophobic we coated its surface with Pluronic by an overnight incubation in 2% w/w F127 in water.

### Clamping

To confine active microtubules in a predesigned confinement, the patterned COC substrate was loaded with active microtubules, and subsequently covered with a 101-μm thick COC film (TOPAS Advanced Polymers). To prevent leakage or sample drying, the COC layers were sandwiched between a pair of aluminum frames held together by screws and bolts (Fig. S5). The middle of the aluminum frames had a one-inch window to serve as an observation window. To prevent chips from falling through the windows, glass slides were placed across the windows. To even clamping pressure distribution, thin PDMS slabs were inserted between the COC chips and glass slides. After clamping, the samples remained sealed and hydrated for days. Microfluidic chambers were reused after cleaning with ethanol and 20-min sonication in water.

### Analysis of fluid flows

Motion of active fluid flows was quantified by tracking the motion of tracer beads. To measure velocity field, $\mathbf{v}(r, \theta, t)$, we analyzed sequential images of tracer beads with particle image velocimetry (PIV, PIVlab version 1.4) (*57*). Taking curl of velocity field yields vorticity distribution, $c(r, \theta, t) \equiv [\nabla \times \mathbf{v}]_z$. Flows are faster in a larger channel (Fig. 2C, 2D). To compare flow fields and vorticity maps among samples, we normalize velocity fields by their instant spatially averaged speed: $\mathbf{V}(r, \theta, t) \equiv \mathbf{v}(r, \theta, t)/\langle|\mathbf{v}(r, \theta, t)|\rangle_{r,\theta}$, and vorticity distributions by triple their instant standard deviations: $C(r, \theta, t) \equiv c(r, \theta, t)/[3\sigma(t)]$, where $\sigma(t)$ is the standard deviation of a vorticity distribution at time, $t$. To measure flow profile across a channel, tracers were tracked with Lagrangian particle tracking (*58*). Flow profiles were determined by averaging the θ-component of their velocities, $v_\theta$ over time ($t$), and orientations ($\hat{\boldsymbol{\theta}}$): $\langle v_\theta(r, \theta, t)\rangle_{\theta,t}$. To characterize flow coherency, we defined circulation order parameter, Φ as $\Phi \equiv \langle v_\theta/|\mathbf{v}|\rangle$, where $\mathbf{v}$ is tracer velocity. Φ = 1 implies a perfect counter-clockwise flow ($\hat{\boldsymbol{\theta}}$); Φ = −1, clockwise ($-\hat{\boldsymbol{\theta}}$). Φ = 0 implies either random flows or perfect radial flows ($\hat{\mathbf{r}}$)(not seen).

### Elastomer confinements

To ensure that the development of coherent flows is not exclusive to COC-based microfluidic channels, we have confined active fluids in 3D tori inscribed in an elastomer (*59*). The elastomer consisted of 26% w/w 10-cst PDMS oil (Sigma-Aldrich, 378321-250ML) and 74% w/w elastomer (Dow Corning 9041 silicone elastomer blend). To inscribe a torus, we inserted a 27-gauge blunt needle (SAI Infusion Technologies, B27-150) into the elastomer, followed by rotating the elastomer while pumping active fluids through the needle. The pumped fluid formed a torus after one full revolution. The torus radius could be tuned by changing the distance between the needle tip and the elastomer rotation axis; the torus thickness by controlling the pumped fluid volume. Subsequently, the needle was extracted from the elastomer, yielding an isolated torus sealed within the elastomer (Fig. S4). Active fluid contained Pluronic

that coated the inner torus surface, preventing microtubules adsorption. Unlike COC, the elastomer contains PDMS oil so the surface of the torus confinement is fluid.

### Tube confinements

To investigate the broader applicability of our findings we loaded active fluids into a plastic tube [Scientific Commodities Inc., BB31695-PE/5, (Fig. 6)]. The tube length was 1,060 mm; its outer and inner diameters were 1.32 and 0.86 mm, respectively. Tube ends were joined with a 50-mm long 20 gauge metallic needle (SAI infusion technologies, B20-150). The needle outer and inner diameters were 0.91 and 0.60 mm, respectively. To reduce evaporation from gaps between the needle and tube, we applied vacuum grease (Dow Corning). For imaging purpose the tube was fixed on a glass slide with tape. The tube cross-sectional profile was circular, distorting tracer images due to index of refraction mismatch. To reduce such distortions, the tube was immersed in uncured UV glue.

### Analyzing structure of active networks

To correlate fluid flow with underlying active gel structure we z-scan microtubule networks with confocal microscopy when in coherent and turbulent states. From the midplane slice (thickness = 10 μm) we use a filament tracking algorithm to extract bundle structures, represented as winding snakes (magenta curves in Fig. S6A and Movie 8) (*44*). Snakes are composed of unit-length bundle segments whose $r\underline{\theta}$-plane orientations are given by angle $\Psi$, where $-\pi/2 \le \Psi \le \pi/2$. To measure time-averaged distributions of $\underline{\Psi}$, the 3D confocal images of the networks structure were continuously acquired, and from here angles $\underline{\Psi}$ were extracted. The snake reconstruction algorithm has a bias that yields a slight peak around $\underline{\Psi} \sim 0$ and $\pi/2$, even for suspensions that are known to be isotropic (blue curve in Fig. S6B). When the images were rotated by −45° the peaks also shifted by ~45°, demonstrating the biased detection associated with the reconstruction algorithm. To remove this artificial bias we rotated the images from 0° to 360°, by 30° (Fig. S6C). From these images, we extracted and stacked bundle orientations. The stacked orientations yielded a probability orientation distribution to within a few percent (gray curve). Repeating the same experiments with different samples yielded similar distributions (black curve). This method was applied to eliminate the bias of the reconstruction algorithm, for both coherent and incoherent samples (Fig. 7, A and B).

To characterize bundle orientational order we measured the scalar nematic order parameter (NOP), the largest eigenvalue of the nematic order parameter tensor, $Q_{ij}$, defined as $Q_{ij} \equiv \langle \hat{n}_i \hat{n}_j - \delta_{ij}/2 \rangle$, where $\hat{\mathbf{n}} \equiv \cos(\Psi)\hat{\boldsymbol{\theta}} + \sin(\Psi)\hat{\mathbf{r}}$ is the director of a bundle segment, and $\delta_{ij}$ is Kronecker delta function (Fig. S6A). To characterize NOP spatial distribution we measure its radial profile, NOP $(d_o)$; the corresponding tensor profile $Q_{ij}(d_o)$ is measured by taking the average over $t$ and $\underline{\theta}$: $Q_{ij}(d_0) = \langle \cdots \rangle_{t,\theta}$. In either coherent or incoherent states the NOP profile decays from boundaries. The decay length $l$ is defined by where NOP is reduced by a factor of three: NOP (distance $l$ from a boundary) ≡ NOP (at the boundary)/3 (Fig. 7C).

### REFERENCES AND NOTES


1. M. C. Cross, P. C. Hohenberg, Pattern formation outside of equilibrium. *Rev. Mod. Phys.* **65**, 851–1112 (1993). doi: 10.1103/RevModPhys.65.851
2. J. Prost, F. Jülicher, J. Joanny, Active gel physics. *Nat. Phys.* **11**, 111–117 (2015). doi: 10.1038/nphys3224
3. J. Brugués, D. Needleman, Physical basis of spindle self-organization. *Proc. Natl. Acad. Sci. U.S.A.* **111**, 18496–18500 (2014). doi: 10.1073/pnas.1409404111; pmid: 25468965
4. S. R. Naganathan, S. Fürthauer, M. Nishikawa, F. Jülicher, S. W. Grill, Active torque generation by the actomyosin cell cortex drives left-right symmetry breaking. *eLife* **3**, e04165 (2014). doi: 10.7554/eLife.04165; pmid: 25517077
5. Y. H. Tee *et al.*, Cellular chirality arising from the self-organization of the actin cytoskeleton. *Nat. Cell Biol.* **17**, 445–457 (2015). doi: 10.1038/ncb3137; pmid: 25799062
6. K. Doxzen *et al.*, Guidance of collective cell migration by substrate geometry. *Integr. Biol. (Camb.)* **5**, 1026–1035 (2013). doi: 10.1039/c3ib40054a; pmid: 23784144
7. J. Ranft *et al.*, Fluidization of tissues by cell division and apoptosis. *Proc. Natl. Acad. Sci. U.S.A.* **107**, 20863–20868 (2010). doi: 10.1073/pnas.1011086107; pmid: 21078958
8. A. Kumar, A. Maitra, M. Sumit, S. Ramaswamy, G. V. Shivashankar, Actomyosin contractility rotates the cell nucleus. *Sci. Rep.* **4**, 3781 (2014). doi: 10.1038/srep03781; pmid: 24445418
9. I. H. Riedel, K. Kruse, J. Howard, A self-organized vortex array of hydrodynamically entrained sperm cells. *Science* **309**, 300–303 (2005). doi: 10.1126/science.1110329; pmid: 16002619
10. J. Buhl *et al.*, From disorder to order in marching locusts. *Science* **312**, 1402–1406 (2006). doi: 10.1126/science.1125142; pmid: 16741126
11. R. Di Leonardo, *et al.*, Bacterial ratchet motors. *Proceedings of the National Academy of Sciences* **107**, 9541-9545 (2010).
12. H. Wioland, F. G. Woodhouse, J. Dunkel, J. O. Kessler, R. E. Goldstein, Confinement stabilizes a bacterial suspension into a spiral vortex. *Phys. Rev. Lett.* **110**, 268102 (2013). doi: 10.1103/PhysRevLett.110.268102; pmid: 23848925
13. F. G. Woodhouse, R. E. Goldstein, Spontaneous circulation of confined active suspensions. *Phys. Rev. Lett.* **109**, 168105 (2012). doi: 10.1103/PhysRevLett.109.168105; pmid: 23215137
14. H. H. Wensink *et al.*, Meso-scale turbulence in living fluids. *Proc. Natl. Acad. Sci. U.S.A.* **109**, 14308–14313 (2012). doi: 10.1073/pnas.1202032109; pmid: 22908244
15. A. Sokolov, M. M. Apodaca, B. A. Grzybowski, I. S. Aranson, Swimming bacteria power microscopic gears. *Proc. Natl. Acad. Sci. U.S.A.* **107**, 969–974 (2010). doi: 10.1073/pnas.0913015107; pmid: 20080560
16. A. Creppy *et al.*, Symmetry-breaking phase transitions in highly concentrated semen. *J. R. Soc. Interface* **13**, 20160575 (2016). doi: 10.1098/rsif.2016.0575; pmid: 27733694
17. H. Wioland, E. Lushi, R. E. Goldstein, Directed collective motion of bacteria under channel confinement. *New J. Phys.* **18**, 075002 (2016). doi: 10.1088/1367-2630/18/7/075002
18. M. Marchetti *et al.*, Hydrodynamics of soft active matter. *Rev. Mod. Phys.* **85**, 1143–1189 (2013). doi: 10.1103/RevModPhys.85.1143
19. D. Saintillan, M. J. Shelley, Active suspensions and their nonlinear models. *C. R. Phys.* **14**, 497–517 (2013). doi: 10.1016/j.crhy.2013.04.001
20. J. Toner, Y. Tu, S. Ramaswamy, Hydrodynamics and phases of flocks. *Ann. Phys.* **318**, 170–244 (2005). doi: 10.1016/j.aop.2005.04.011
21. J. Palacci, S. Sacanna, A. P. Steinberg, D. J. Pine, P. M. Chaikin, Living crystals of light-activated colloidal surfers. *Science* **339**, 936–940 (2013). doi: 10.1126/science.1230020; pmid: 23371555
22. V. Schaller, C. Weber, C. Semmrich, E. Frey, A. R. Bausch, Polar patterns of driven filaments. *Nature* **467**, 73–77 (2010). doi: 10.1038/nature09312; pmid: 20811454
23. I. Theurkauff, C. Cottin-Bizonne, J. Palacci, C. Ybert, L. Bocquet, Dynamic clustering in active colloidal suspensions with chemical signaling. *Phys. Rev. Lett.* **108**, 268303 (2012). doi: 10.1103/PhysRevLett.108.268303; pmid: 23005020
24. T. Sanchez, D. T. N. Chen, S. J. DeCamp, M. Heymann, Z. Dogic, Spontaneous motion in hierarchically assembled active matter. *Nature* **491**, 431–434 (2012). doi: 10.1038/nature11591; pmid: 23135402
25. S. Zhou, A. Sokolov, O. D. Lavrentovich, I. S. Aranson, Living liquid crystals. *Proc. Natl. Acad. Sci. U.S.A.* **111**, 1265–1270 (2014). doi: 10.1073/pnas.1321926111; pmid: 24474746
26. Y. Fily, M. C. Marchetti, Athermal phase separation of self-propelled particles with no alignment. *Phys. Rev. Lett.* **108**, 235702 (2012). doi: 10.1103/PhysRevLett.108.235702; pmid: 23003972
27. S. Fürthauer, M. Neef, S. Grill, K. Kruse, F. Jülicher, The Taylor–Couette motor: Spontaneous flows of active polar fluids between two coaxial cylinders. *New J. Phys.* **14**, 023001 (2012). doi: 10.1088/1367-2630/14/2/023001
28. R. Voituriez, J.-F. Joanny, J. Prost, Spontaneous flow transition in active polar gels. *Europhys. Lett.* **70**, 404–410 (2005). doi: 10.1209/epl/i2004-10501-2
29. J. Stenhammar, R. Wittkowski, D. Marenduzzo, M. E. Cates, Light-induced self-assembly of active rectification devices. *Sci. Adv.* **2**, e1501850 (2016). doi: 10.1126/sciadv.1501850; pmid: 27051883
30. S. P. Thampi, A. Doostmohammadi, T. N. Shendruk, R. Golestanian, J. M. Yeomans, Active micromachines: Microfluidics powered by mesoscale turbulence. *Sci. Adv.* **2**, e1501854 (2016). doi: 10.1126/sciadv.1501854; pmid: 27419229
31. A. Bricard, J.-B. Caussin, N. Desreumaux, O. Dauchot, D. Bartolo, Emergence of macroscopic directed motion in populations of motile colloids. *Nature* **503**, 95–98 (2013). doi: 10.1038/nature12673; pmid: 24201282
32. H. M. López, J. Gachelin, C. Douarche, H. Auradou, E. Clément, Turning Bacteria Suspensions into Superfluids. *Phys. Rev. Lett.* **115**, 028301 (2015). doi: 10.1103/PhysRevLett.115.028301; pmid: 26207507
33. G. K. Batchelor, *An Introduction to Fluid Dynamics* (Cambridge Univ. Press, 2000).
34. L. R. Serbus, B.-J. Cha, W. E. Theurkauf, W. M. Saxton, Dynein and the actin cytoskeleton control kinesin-driven cytoplasmic streaming in *Drosophila* oocytes. *Development* **132**, 3743–3752 (2005). doi: 10.1242/dev.01956; pmid: 16077093
35. F. G. Woodhouse, R. E. Goldstein, Cytoplasmic streaming in plant cells emerges naturally by microfilament self-organization. *Proc. Natl. Acad. Sci. U.S.A.* **110**, 14132–14137 (2013). doi: 10.1073/pnas.1302736110; pmid: 23940314
36. T. E. Schroeder, D. E. Battaglia, "Spiral asters" and cytoplasmic rotation in sea urchin eggs: Induction in *Strongylocentrotus purpuratus* eggs by elevated temperature. *J. Cell Biol.* **100**, 1056–1062 (1985). doi: 10.1083/jcb.100.4.1056; pmid: 3156865
37. E. Lushi, H. Wioland, R. E. Goldstein, Fluid flows created by swimming bacteria drive self-organization in confined suspensions. *Proc. Natl. Acad. Sci. U.S.A.* **111**, 9733–9738 (2014). doi: 10.1073/pnas.1405698111; pmid: 24958878
38. G. Henkin, S. J. DeCamp, D. T. N. Chen, T. Sanchez, Z. Dogic, Tunable dynamics of microtubule-based active isotropic gels. *Philos. Trans. A Math. Phys. Eng. Sci.* **372**, 20140142 (2014). doi: 10.1098/rsta.2014.0142; pmid: 25332391
39. F. J. Nédélec, T. Surrey, A. C. Maggs, S. Leibler, Self-organization of microtubules and motors. *Nature* **389**, 305–308 (1997). doi: 10.1038/38532; pmid: 9305848
40. T. Surrey, F. Nédélec, S. Leibler, E. Karsenti, Physical properties determining self-organization of motors and microtubules. *Science* **292**, 1167–1171 (2001). doi: 10.1126/science.1059758; pmid: 11349149
41. F. Hilitski *et al.*, Measuring cohesion between macromolecular filaments one pair at a time: Depletion-induced microtubule bundling. *Phys. Rev. Lett.* **114**, 138102 (2015). doi: 10.1103/PhysRevLett.114.138102; pmid: 25884139
42. C. Hentrich, T. Surrey, Microtubule organization by the antagonistic mitotic motors kinesin-5 and kinesin-14. *J. Cell Biol.* **189**, 465–480 (2010). doi: 10.1083/jcb.200910125; pmid: 20439998
43. E. Pairam, A. Fernández-Nieves, Generation and stability of toroidal droplets in a viscous liquid. *Phys. Rev. Lett.* **102**, 234501 (2009). doi: 10.1103/PhysRevLett.102.234501; pmid: 19658939
44. T. Xu *et al.*, SOAX: A software for quantification of 3D biopolymer networks. *Sci. Rep.* **5**, 9081 (2015). doi: 10.1038/srep09081; pmid: 25765313

45. R. Aditi Simha, S. Ramaswamy, Hydrodynamic fluctuations and instabilities in ordered suspensions of self-propelled particles. *Phys. Rev. Lett.* **89**, 058101 (2002). doi: 10.1103/PhysRevLett.89.058101; pmid: 12144468
46. D. van der Beek *et al.*, Isotropic-nematic interface and wetting in suspensions of colloidal platelets. *Phys. Rev. Lett.* **97**, 087801 (2006). doi: 10.1103/PhysRevLett.97.087801; pmid: 17026337
47. A. Hurd, S. Fraden, F. Lonberg, R. Meyer, Field-induced transient periodic structures in nematic liquid crystals: The splay Frederiks transition. *J. Phys.* **46**, 905–917 (1985). doi: 10.1051/jphys:01985004606090500
48. P. Pieranski, F. Brochard, E. Guyon, Static and dynamic behavior of a nematic liquid crystal in a magnetic field. Part II: Dynamics. *J. Phys.* **34**, 35–48 (1973). doi: 10.1051/jphys:0197300340103500
49. L. Giomi, M. C. Marchetti, T. B. Liverpool, Complex spontaneous flows and concentration banding in active polar films. *Phys. Rev. Lett.* **101**, 198101 (2008). doi: 10.1103/PhysRevLett.101.198101; pmid: 19113315
50. D. Marenduzzo, E. Orlandini, M. E. Cates, J. M. Yeomans, Steady-state hydrodynamic instabilities of active liquid crystals: Hybrid lattice Boltzmann simulations. *Phys. Rev. E Stat. Nonlin. Soft Matter Phys.* **76**, 031921 (2007). doi: 10.1103/PhysRevE.76.031921; pmid: 17930285
51. B. J. Kirby, *Micro-and Nanoscale Fluid Mechanics: Transport in Microfluidic Devices* (Cambridge Univ. Press, 2010).
52. D. S. Martin, R. Fathi, T. J. Mitchison, J. Gelles, FRET measurements of kinesin neck orientation reveal a structural basis for processivity and asymmetry. *Proc. Natl. Acad. Sci. U.S.A.* **107**, 5453–5458 (2010). doi: 10.1073/pnas.0914924107; pmid: 20212149
53. M. Castoldi, A. V. Popov, Purification of brain tubulin through two cycles of polymerization-depolymerization in a high-molarity buffer. *Protein Expr. Purif.* **32**, 83–88 (2003). doi: 10.1016/S1046-5928(03)00218-3; pmid: 14680943
54. T. G. Huang, D. D. Hackney, *Drosophila* kinesin minimal motor domain expressed in Escherichia coli. Purification and kinetic characterization. *J. Biol. Chem.* **269**, 16493–16501 (1994). pmid: 8206959
55. G. Wanka, H. Hoffmann, W. Ulbricht, Phase diagrams and aggregation behavior of poly(oxyethylene)-poly(oxypropylene)-poly(oxyethylene) triblock copolymers in aqueous solutions. *Macromolecules* **27**, 4145–4159 (1994). doi: 10.1021/ma00093a016
56. S. A. Aghvami *et al.*, Rapid prototyping of cyclic olefin copolymer (COC) microfluidic devices. *Sens. Actuators B Chem.* 10.1016/j.snb.2017.03.023 (2017). doi: 10.1016/j.snb.2017.03.023
57. W. Thielicke, E. J. Stamhuis, PIVlab–Towards user-friendly, affordable and accurate digital particle image velocimetry in MATLAB. *J. Open Res. Softw.* **2**, e30 (2014). doi: 10.5334/jors.bl
58. N. T. Ouellette, H. Xu, E. Bodenschatz, A quantitative study of three-dimensional Lagrangian particle tracking algorithms. *Exp. Fluids* **40**, 301–313 (2005). doi: 10.1007/s00348-005-0068-7
59. E. Pairam, H. Le, A. Fernández-Nieves, Stability of toroidal droplets inside yield stress materials. *Phys. Rev. E Stat. Nonlin. Soft Matter Phys.* **90**, 021002 (2014). doi: 10.1103/PhysRevE.90.021002; pmid: 25215681



## ACKNOWLEDGMENTS

This work was primarily supported by the U.S. Department of Energy, Office of Basic Energy Sciences, through award DE-SC0010432TDD (K.T.W., S.J.D., and Z.D.). We also acknowledge support by NSF-MRSEC-1420382 (J.B.H. and S.F.). We acknowledge use of the Brandeis Materials Research Science and Engineering Center (MRSEC) optical, microfluidic, and biosynthesis facilities supported by NSF-MRSEC-1420382. Analysis of microtubule networks was supported by Templeton Foundation grant 57392 (D.T.N.C). We acknowledge B. Rogers for use of his confocal microscope. We are grateful to D. Needleman for providing historical perspective on self-organized machines. K.-T.W. performed the research; J.B.H. acquired data in micrometer confinements; K.-T.W., J.B.H., S.F., and Z.D. analyzed the data; D.T.N.C. analyzed the network structure; Z.D. and S.F. designed the research; S.J.D, K.-T.W, Y.W.C., and A.F.-N. observed the initial effects; and K.-T.W., S.F., and Z.D. wrote the manuscript. All authors have reviewed the manuscript.


## SUPPLEMENTARY MATERIALS

www.sciencemag.org/content/355/6331/eaal1979/suppl/DC1
Materials and Methods
Figs. S1 to S6

12 October 2016; accepted 10 February 2017
10.1126/science.aal1979

**Transition from turbulent to coherent flows in confined three-dimensional active fluids**

Kun-Ta Wu, Jean Bernard Hishamunda, Daniel T. N. Chen, Stephen J. DeCamp, Ya-Wen Chang, Alberto Fernández-Nieves, Seth Fraden and Zvonimir Dogic (March 23, 2017)

*Science* **355** (6331), . [doi: 10.1126/science.aal1979]

Editor's Summary

**Go with the changing flow**

The transport of ordinary fluids tends to be driven by pressure differentials, whereas for active or biological matter, transport may be isotropic or governed by the presence of specific chemical gradients. Wu *et al.* analyzed the emergence of spontaneous directional flows in active fluids containing a suspension of microtubules and clusters of the molecular motor kinesin, confined in a variety of microfluidic geometries (see the Perspective by Morozov). When confined in periodic toroidal channels and cylindrical domains, the flow was organized and persisted in a unidirectional motion, either clockwise or counterclockwise. Oddly, this behavior was independent of scale; as long as the aspect ratio of the geometry was chosen appropriately, flows were observed for a wide range of system dimensions.

*Science*, this issue p. eaal1979; see also p. 1262



*Science* (print ISSN 0036-8075; online ISSN 1095-9203) is published weekly, except the last week in December, by the American Association for the Advancement of Science, 1200 New York Avenue NW, Washington, DC 20005. 

www.sciencemag.org/content/355/6331/eaal1979/suppl/DC1

# Supplementary Material for

## Transition from turbulent to coherent flows in confined three-dimensional active fluids

Kun-Ta Wu, Jean Bernard Hishamunda, Daniel T. N. Chen, Stephen J. DeCamp, Ya-Wen Chang, Alberto Fernández-Nieves, Seth Fraden,* Zvonimir Dogic*

*Corresponding author. Email: fraden@brandeis.edu (S.F.); zdogic@brandeis.edu (Z.D.)

Published 24 March 2017, *Science* **355**, eaal1979 (2017)
DOI: 10.1126/science.aal1979

**This PDF file includes:**

Figs. S1 to S6

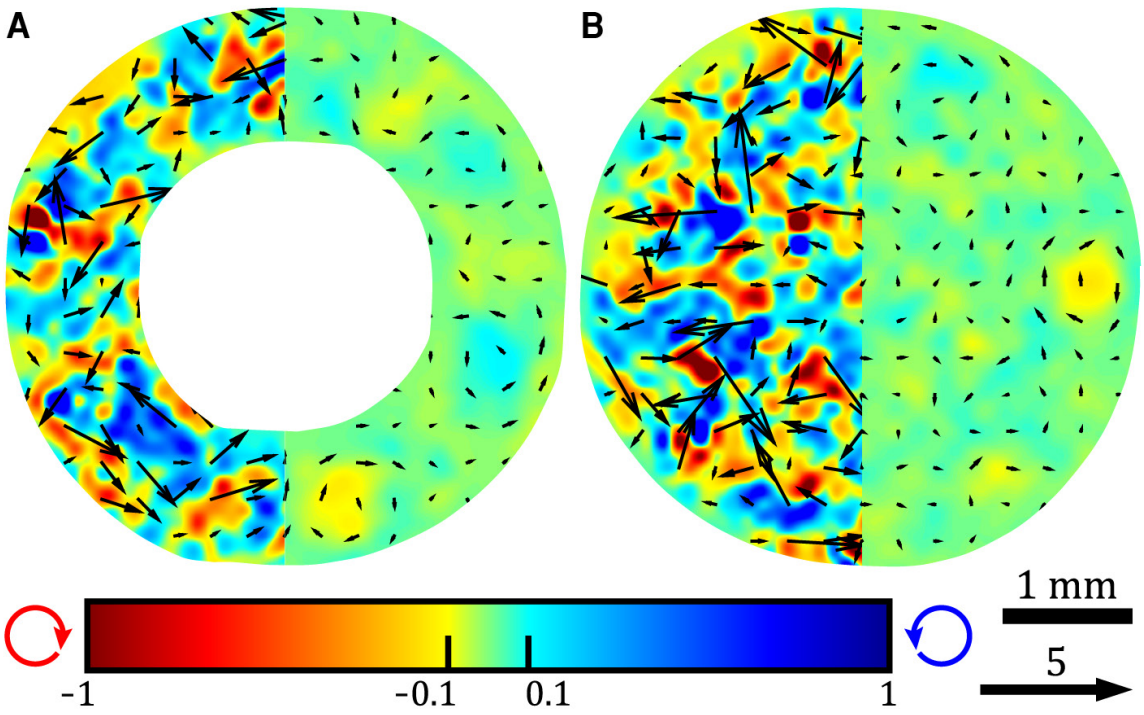


**Fig. S1. Geometrical confinements with large aspect ratios suppress coherent flows.** **(A)** Incoherent flow in a toroidal geometry, with low circulation order parameter ($\Phi$ = 0.02). Coherent flows were suppressed by reducing the height of the confining geometry from 1.3 to 0.33 mm (Fig. 1E). **(B)** Incoherent flow in cylinder with low circulation order parameter ($\Phi$ = 0.03). To suppress coherent flows the height was reduced from 1.3 to 0.33 mm (Fig. 1F).

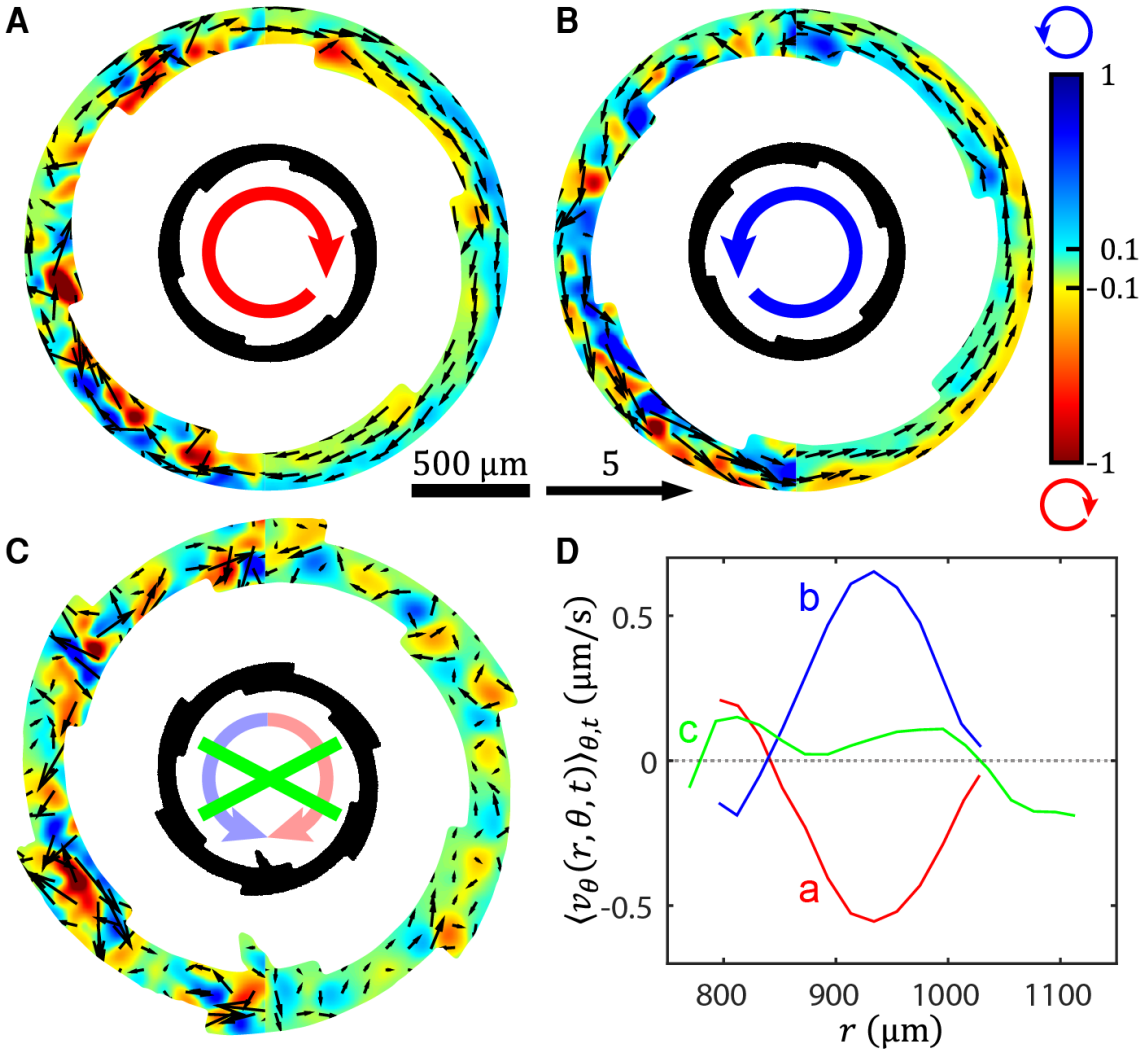


**Fig. S2**

**Ratchet geometries that suppress coherent flows.** (**A**) Clockwise circular flow directed by counter-clockwise saw-teeth decorating the inner toroid surface. Channel height is 70 µm. (**B**) Clockwise notches on the inner toroid surface direct counter-clockwise circulation. (**C**) Inner and outer saw-teeth patterns of the same handedness induce flows with the opposite handiness (Fig. 3A), consequently suppressing coherent flows. (**D**) Velocity profiles of the self-organized flows in geometries shown in panels A-C.

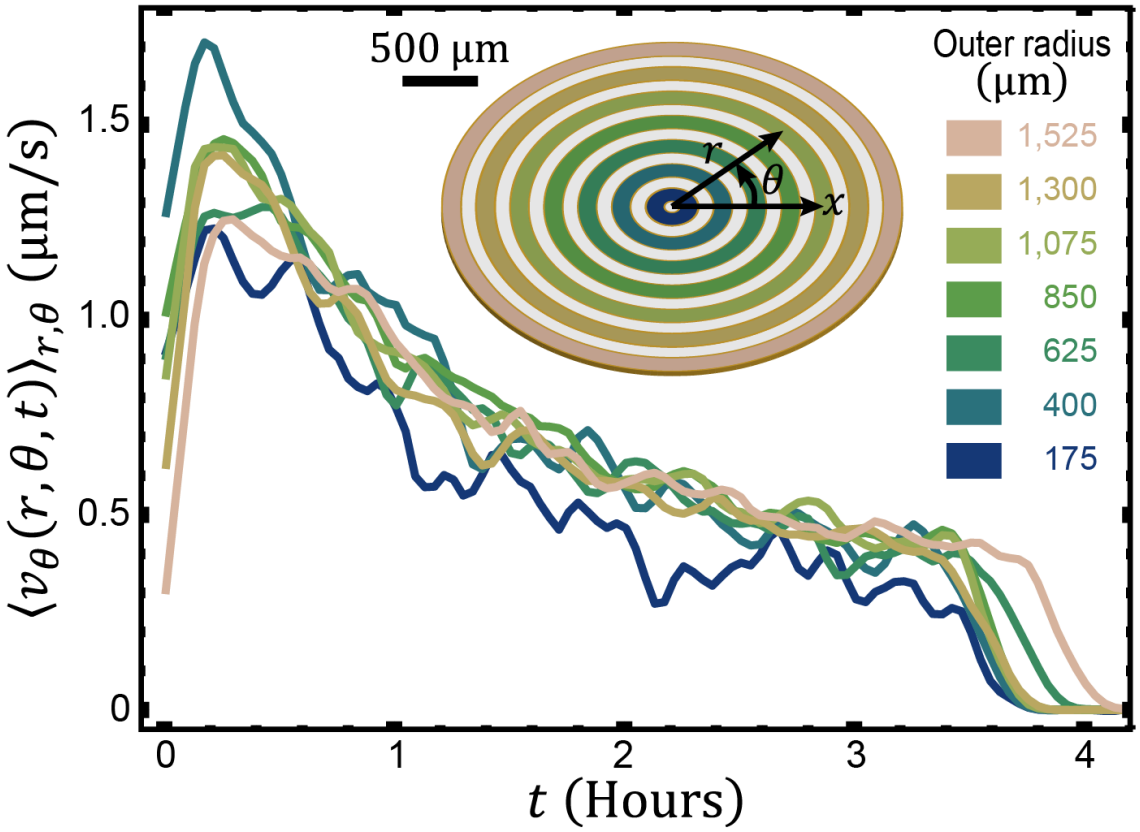


**Fig. S3 Flow profiles are independent of the toroid radius and curvature.** Evolution of the mean azimuthal velocities plotted for seven concentric toroids whose radii range from 175 to 1,525 μm. Flow velocities in toroids with different radii evolve similarly, demonstrating that the coherent flows are independent of the confinement curvature. Toroid heights are 60 μm.

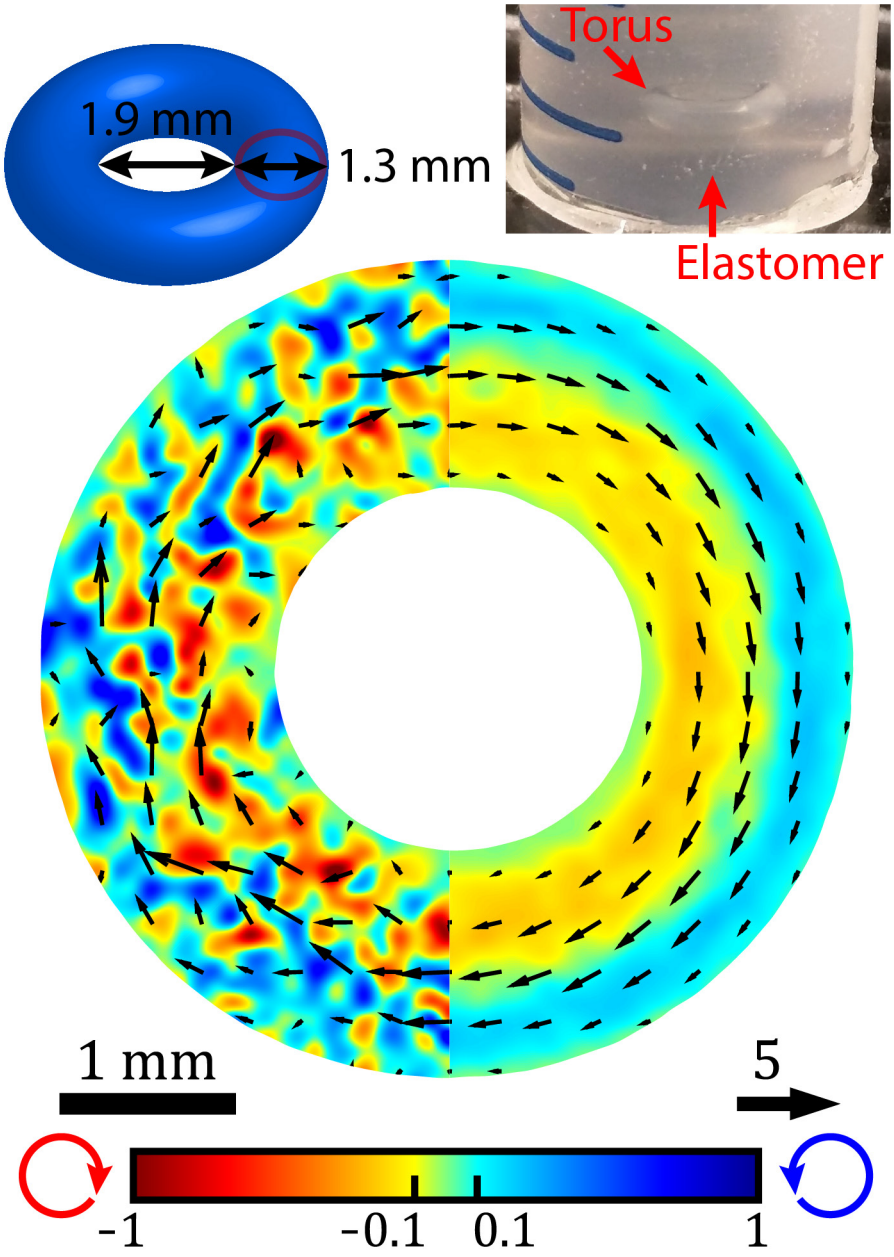


**Fig. S4 Coherent flows confined in elastomers.** Self-organized flows of an active fluid are confined within a torus inscribed in an elastomer. The active fluid develops a coherent clockwise circulation.

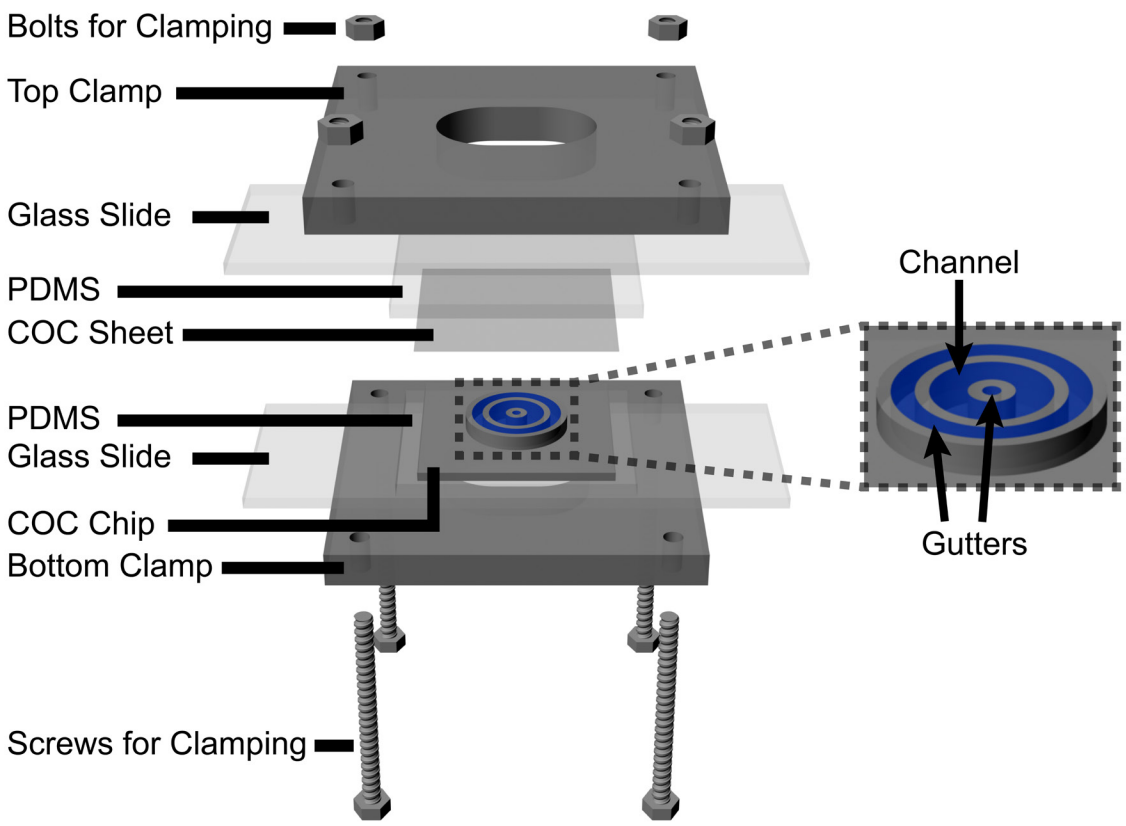


**Fig. S5 Clamping a microfluidic device for confining active microtubules.** To prevent evaporation the device is sealed with a clamp; the sample remains hydrated for days.

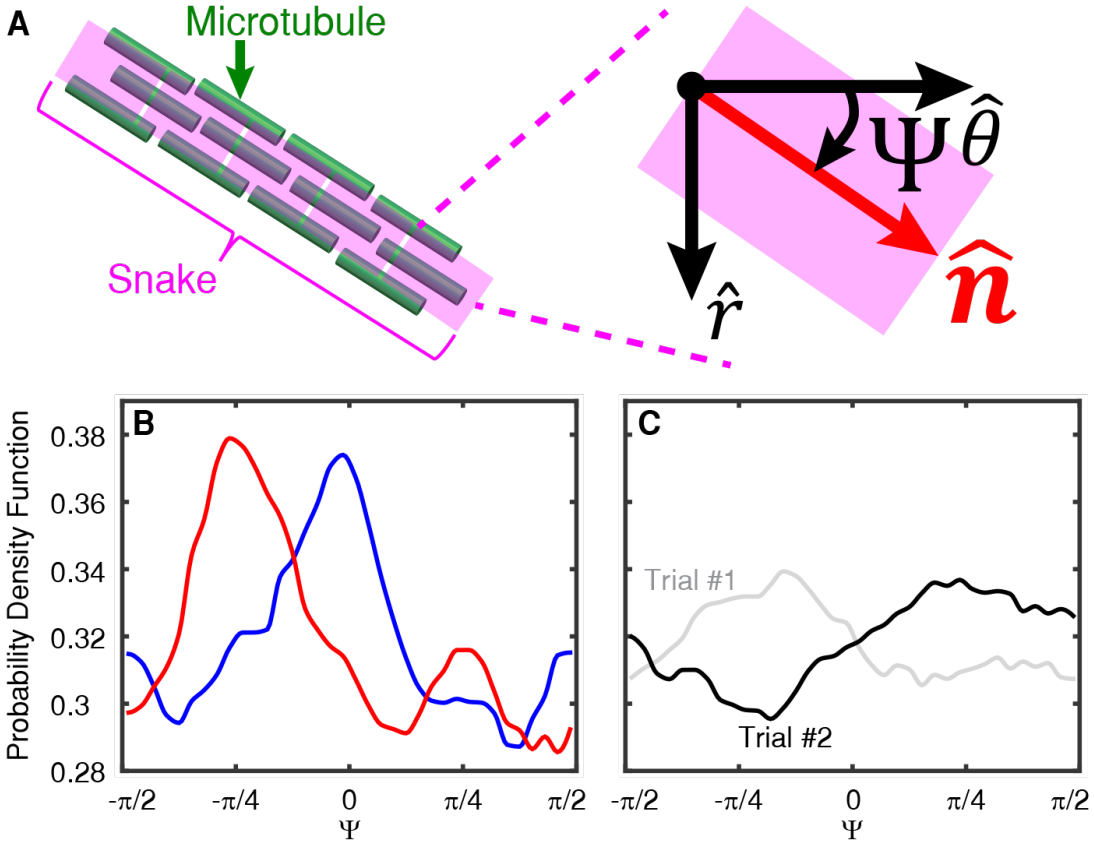


**Fig. S6 Orientational distribution of bundle segments in an isotropic suspension. (A)** Microtubule network structures is described by snakes, composed of unit length segments. Segment orientations in the x-y plane are characterized by director, $\hat{\mathbf{n}}$, angled to $\hat{\theta}$-axis by $\Psi$. **(B)** The distribution of bundle segments from the original (blue) and (-π/4)-rotated (red) 3D images demonstrates that the network reconstruction algorithm has a slight bias for detecting segments that are preferentially aligned along 0 and π/2 degrees. In the red curve both the image and the reference frame is rotated by 45 degrees. The peak shift implies an artifact along image x-y axes. **(C)** The distributions of orientations stacked from one original and eleven structure that are rotated by 30° images. Gray and black curves represent two independent measurements, and the probability distribution function is flat to within a few percent. The isotropic suspension is confined in a cuboid whose length, width and height are 18,000, 14,000 and 90 μm, respectively.